

*Army Research Laboratory*



**Day-24: Energy Balance Model  
for Infrared Scene Generation**

**By  
Robert A. Sutherland**

**U.S. Army Research Laboratory  
Survivability/Lethality Analysis Directorate**

**ARL-TR-2672**

**April 2002**

Approved for public release; distribution unlimited.

**20020507 224**

## NOTICES

### Disclaimers

The findings in this report are not to be construed as an official Department of the Army position, unless so designated by other authorized documents.

Citation of manufacturers' or trade names does not constitute an official endorsement or approval of the use thereof.

DESTRUCTION NOTICE—When this document is no longer needed, destroy it by any method that will prevent disclosure of its contents or reconstruction of the document.

<b>REPORT DOCUMENTATION PAGE</b>			<i>Form Approved</i> <b>OMB No. 0704-0188</b>	
Public reporting burden for this collection of information is estimated to average 1 hour per response, including the time for reviewing instructions, searching existing data sources, gathering and maintaining the data needed, and completing and reviewing the collection information. Send comments regarding this burden estimate or any other aspect of this collection of information, including suggestions for reducing the burden, to Department of Defense, Washington Headquarters Services, Directorate for Information Operations and Reports (0704-0188), 1215 Jefferson Davis Highway, Suite 1204, Arlington, VA 22202-4302. Respondents should be aware that notwithstanding any other provision of law, no person shall be subject to any penalty for failing to comply with a collection of information if it does not display a currently valid OMB control number. <b>PLEASE DO NOT RETURN YOUR FORM TO THE ABOVE ADDRESS.</b>				
<b>1. REPORT DATE (DD-MM-YYYY)</b> April 2002		<b>2. REPORT TYPE</b> Final		<b>3. DATES COVERED (From - To)</b> September 2001-February 2002
<b>4. TITLE AND SUBTITLE</b> DAY-24: Energy Balance Model for Infrared Scene Generation			<b>5a. CONTRACT NUMBER</b>	
			<b>5b. GRANT NUMBER</b>	
			<b>5c. PROGRAM ELEMENT NUMBER</b>	
<b>6. AUTHOR(S)</b> Sutherland, Robert A.			<b>5d. PROJECT NUMBER</b>	
			<b>5e. TASK NUMBER</b>	
			<b>5f. WORK UNIT NUMBER</b>	
<b>7. PERFORMING ORGANIZATION NAME(S) AND ADDRESS(ES)</b> U.S. Army Research Laboratory Information and Electronic Protection Division Survivability Lethality Analysis Directorate (ATTN: AMSRL-SL-EM) White Sands Missile Range, NM 88002-5513			<b>8. PERFORMING ORGANIZATION REPORT NUMBER</b>  ARL-TR-2672	
<b>9. SPONSORING/MONITORING AGENCY NAME(S) AND ADDRESS(ES)</b> U.S. Army Research Laboratory 2800 Powder Mill Road Adelphi, MD 20783-1145			<b>10. SPONSOR/MONITOR'S ACRONYM(S)</b>	
			<b>11. SPONSOR/MONITOR'S REPORT NUMBER(S)</b>  ARL-TR-2672	
<b>12. DISTRIBUTION/AVAILABILITY STATEMENT</b> Approved for public release; distribution unlimited				
<b>13. SUPPLEMENTARY NOTES</b>				
<b>14. ABSTRACT</b> We expand and modify the Rachele-Tunick "energy balance" concept to include infrared thermal scenes and dynamic effects over time periods of several diurnal cycles. The model requires an initial starting "IR image" in the form of a two-dimensional temperature array of the scene (generated either synthetically or from real data) plus four corresponding land-use maps describing, (1) surface shortwave reflectivity, (2) longwave emissivity, (3) vegetation type, and (4) subsurface thermal conductivity, some of which can also be generated from empirical models. Meteorological inputs are required at only one key location inside the scene area. These inputs include air temperature, wind speed, relative humidity, cloud cover, and subsurface "deep soil" temperature. Incoming shortwave solar/sky radiation and longwave sky radiation are optional inputs. Comparisons with data from field experiments indicate that the simple static, or equilibrium, energy balance model does a surprisingly reasonable job of modeling surface temperature despite some obvious conceptual shortcomings which we address using the more rigorous time dependent formulation.				
<b>15. SUBJECT TERMS</b> energy balance, boundary layer modeling, infrared signatures, radiation balance				
<b>16. SECURITY CLASSIFICATION OF:</b>			<b>17. LIMITATION OF ABSTRACT</b>	<b>18. NUMBER OF PAGES</b>
<b>a. REPORT</b> U	<b>b. ABSTRACT</b> U	<b>c. THIS PAGE</b> U	SAR	48
			<b>19a. NAME OF RESPONSIBLE PERSON</b> R.A. Sutherland	
			<b>19b. TELEPHONE NUMBER (Include area code)</b> (505) 678-4520	

---

## Preface

---

This report documents the underlying equations and methods of the DAY-24 model that is being developed by the U.S. Army Research Laboratory, Survivability Lethality Analysis Directorate (SLAD) to simulate infrared signatures of natural background scenes as affected by atmospheric and meteorological processes. The work is funded as part of the SLAD mission in support of the Tools, Techniques, and Methods thrust in infrared synthetic scene generation and was performed entirely in-house. The model was developed to meet the requirements of SLAD System Leaders in tasks to evaluate various countermeasure technologies being developed for hit avoidance and target acquisition.

---

## Acknowledgements

---

We acknowledge the contributions of the Survivability/Lethality Analysis Directorate Field Team for conducting the field experiments and collecting the data for model verification. Specific individuals to be acknowledged are Lon Anderson, Team Leader, Steve Lacy, Met Data, and Thelma Chenault, Data Analysis. Others include Robin Lacy, Rebecca Phillips, Mark Nelson, and Joe Trammel, all students at New Mexico State University. Scarlett Ayres served as the liaison for contributing technical details from the U.S. Army Corps of Engineers Smart Weapons Operability Environment Program and provided the baseline thermal scenes.

---

## Contents

---

Preface	iii
Acknowledgements	v
Executive Summary	ix
1. Introduction	10
2. Earth-Air Surface Formulation	5
3. Equilibrium Surface Fluxes	9
4. Equilibrium Surface Temperature	15
5. Time Dependence	17
6. Application To IR Scene Generation	19
7. Summary	23
8. References	25
Appendix	
A. Parameter Definitions .....	27
Distribution	31

## Figures

1. Sketch of boundary layer model .....	2
2. Expanded sketch of earth-air interface region .....	5
3. DAY-24 meteorological input and modeled fluxes .....	10
4. DAY-24 effect of soil thermal properties.....	12
5. IR scene baseline temperature map (upper) and soil map (lower) .....	19
6. IR scene emissivity map (upper) and reflectivity map (lower) .....	20
7. IR scene diurnal cycle .....	21

---

## Executive Summary

---

This report documents the technical development and validation of the U.S. Army Research Laboratory (ARL), Survivability/Lethality Analysis Directorate (SLAD) thermal infrared (IR) scene model, DAY-24. The model was developed in response to a need in SLAD to predict electromagnetic IR signatures of natural backgrounds of various types under various meteorological and atmospheric conditions. The output of DAY-24 is (1) a detailed "stand alone" surface temperature and "energy balance" single point analysis, and (2) an extended area IR scene, or "signature," which can then serve as a baseline and input for systems effects simulations such as the SLAD Scene and Countermeasure Integration for Munition Interaction with Targets (SCIMITAR) program. The model starts with a known given IR scene and a set of standard meteorological conditions and projects over a full 24-h diurnal cycle or longer. It is required that the standard meteorological conditions be known (from either a posteriori data or from other models) over the full time period and that the extended scene area be reasonably homogeneous. The model addresses the problem in two parts: (1) to predict the surface temperature (and hence signature) at a single point based on the known meteorology and (2) to extrapolate the single point results over the extended scene area. The point model is based upon the equilibrium "energy balance" developed by Rachele and Tunick<sup>1</sup> as part of the ARL Radiation and Energy Balance Field Study project. The model also borrows, in part, from the U.S. Army Corps of Engineers Smart Weapons Operability Environment (SWOE) model<sup>2</sup> for characterizing the extended scene area in terms of surface thermal and radiative properties. The model treats effects of incoming solar and sky radiation, turbulent heat transport, thermal conduction into the (soil) substrate, and evaporative cooling. Results for the single site experiment agree favorably with the SLAD Team measurements and extended area IR scene simulations appear reasonable. Methods for verifying against other models and field measurements are planned.

---

<sup>1</sup> Rachele, H. and A. Tunick, "Energy Balance for Imagery and Electro-magnetic Propagation," *Journal of Applied Meteorology*, 33:8 (1994): 964-976.

<sup>2</sup> Welch, J.P., "Smart Weapons Operability Enhancement Joint Test and Evaluation Program: Final Report," U.S Army Corps of Engineers SWOE Report 94-1, 1994.



---

## 1. Introduction

---

Most of the existing surface "energy balance" models used in meteorological applications are based, for the most part, on the following rigorous relationship relating temperature,  $T$ , to the energy flux density,  $F$ , as

$$\rho C_p \frac{dT(\vec{r}, t)}{dt} = -\nabla \cdot \vec{F}(\vec{r}, t) \quad (1)$$

where the product,  $\rho C_p$ , is the volumetric heat capacity of the medium,  $t$  is time,  $\vec{r}$  denotes location is the usual Cartesian coordinate designation, and  $F$  is the vector heat flux density. It is sometimes convenient for finite element modeling to express eq (1) in the following equivalent integral form as

$$\int_V \rho C_p \frac{dT(\vec{r}, t)}{dt} dV = \int_A (\vec{F} \cdot \hat{n}) dA \quad (2)$$

which follows directly from the mathematical Gauss theorem and applies to any finite volume element  $V$  enclosed by the corresponding surface area  $A$  and where  $\hat{n}$  is the inward directed surface area normal unit vector. In either case the flux density vector is written in most general form as

$$\vec{F}(\vec{r}, t) = \mathbf{R}(\vec{r}, t) + \vec{H}(\vec{r}, t) + \vec{S}(\vec{r}, t) \quad (3)$$

where the three terms on the right account, respectively, for the three major heat energy transfer mechanisms of radiation,  $\mathbf{R}$ , convection,  $\vec{H}$ , and conduction,  $\vec{S}$ .

For the one-dimensional case, used almost universally in modeling the surface energy balance for atmospheric applications, the energy flux vectors are all directed in the vertical, in which case upon inserting eq (3) into either eq (1) or eq (2), we have the more convenient scalar form

$$\rho C_p \frac{dT(z, t)}{dt} = -\left\{ \frac{\partial R(z, t)}{\partial z} + \frac{\partial H(z, t)}{\partial z} + \frac{\partial S(z, t)}{\partial z} \right\} \quad (4)$$

which is valid for any point in the atmosphere or subsurface as long as we use the appropriate values for the specific heat capacity. Equation (4) as written does not include any direct effects of horizontal advection and any latent heat or chemical energy storage terms, but is otherwise valid for any point, provided we used the appropriate values for the thermal properties of the medium.

In any practical model it is convenient to separate the atmosphere-subsurface system into the three regions: the air-atmosphere, subsurface soil, and interface layers (fig. 1). Applying the usual assumptions, eq (4) is expressed in each of the three subregions as

*Atmospheric layer:*

$$(\rho C_p)_{\text{air}} \frac{dT(z, t)}{dt} = -\left\{ \frac{\partial R(z, t)}{\partial z} + \frac{\partial H(z, t)}{\partial z} \right\} \quad (5)$$

*Interface region:*

$$(\rho C_p)_{\text{sfc}} \frac{dT(z, t)}{dt} = \frac{\partial R(z, t)}{\partial z} + \frac{\partial H(z, t)}{\partial z} + \frac{\partial S(z, t)}{\partial z} \quad (6)$$

*Subsurface region:*

$$(\rho C_p)_{\text{sub}} \frac{dT(z, t)}{dt} = -\frac{\partial S(z, t)}{\partial z} \quad (7)$$

where we have explicitly assumed the conduction term to be negligible in the air-atmosphere layer and both the convection and radiative terms to be negligible in the soil subsurface layer (as indicated in fig. 1). The interface is a special case involving all three fluxes that are dissipated in a near infinitesimal layer.

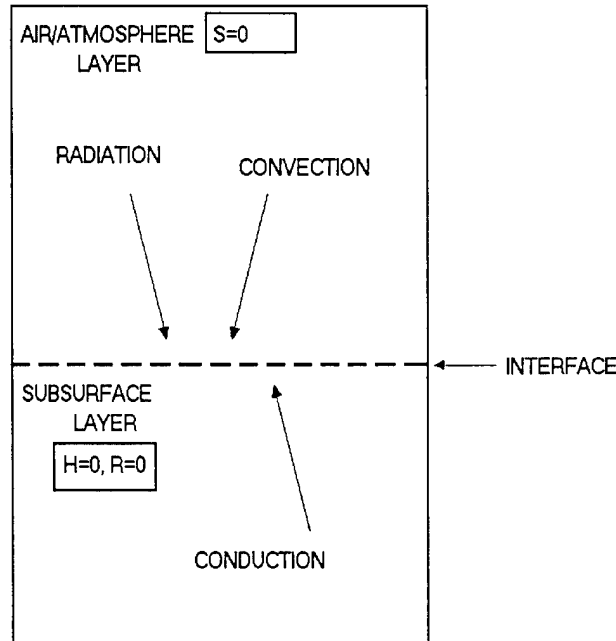


Figure 1. Sketch of the boundary layer model.

The expressions for the atmospheric and subsurface regions (eq (5) and (7)) are well behaved and have been solved in various degrees of approximation elsewhere and will not be further discussed here except when needed for clarification. Our main area of concentration is on the interface region (eq (6)) from which we derive the surface temperature that ultimately serves as a boundary condition for the other regions. In the remainder of the paper, we first apply the above formalism to the earth-air interface for the special case of thermal equilibrium using the general approach described by Rachele and Tunick [1] and then examine the implications of the approach in light of the more rigorous non-equilibrium formulation proposed by Sutherland. [2] We then extend the concept to include an entire IR thermal scene, which we then model over a full diurnal cycle.

## 2. Earth-Air Surface Formulation

Concentrating on the interface region, we proceed by integrating both sides of eq (6) over an arbitrarily small layer,  $\Delta z$ , to ultimately arrive at the following expression for the interface region [2]:

$$\rho C_s \frac{dT}{dt} = R(0, t) + H(0, t) + S(\Delta z, t) \quad (8)$$

$$\dots \approx R(0, t) + H(0, t) + S(0, t)$$

where  $\rho C_s$  is heat capacity per unit area of the subsoil surface. As indicated in the notation, the first two terms on the right represent the radiative and convective fluxes as evaluated at the top of the layer ( $z=0$ ) and the last term represents the conductive flux as evaluated at the bottom of the layer ( $z=\Delta z$ ) (see fig. 2). Here and throughout, for the interface region only, we treat fluxes directed into the layer as positive and fluxes directed out of the layer as negative, as implied in figure 2. This is somewhat different than the usual meteorological convention; however, it is convenient and even necessary in order to maintain strict consistency with physical principles.

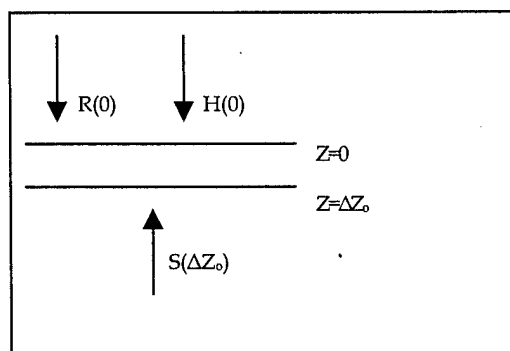


Figure 2. Expanded sketch of the earth-air interface.

The next step is to determine some workable mathematical formulations for the various fluxes in eq (8) with a desire to be as simple as possible. At this point we break from any strictly rigorous formulation and simply accept some of the various semi-empirical parameterization schemes developed over the years by the modeling community; most of which can be found in contemporary texts, for example those by Stull [3] and Jacobs [4].

We begin with the radiation term,  $R(z, t)$ , which is the major driver of the energy balance and includes both a downwelling shortwave

contribution ( $\sim 0.3\text{-}3.0\mu\text{m}$ ) of solar/sky origin and a longwave contribution ( $\sim 3.0\text{-}200.0\mu\text{m}$ ) of thermal origin which includes both the downwelling emissive sky contribution and an upwelling emissive surface contribution, all evaluated at the surface and parameterized as follows:

$$R(0,t) = R_{\text{sun}}(0,t) + R_{\text{sky}}(0,t) + R_{\text{sfc}}(0,t) \quad (9)$$

$$\dots\dots\dots = \{\mu S_o e^{-\tau/\mu} + \mu S_i (1 - e^{-\tau/\mu})\} + \epsilon_{\text{sky}} \sigma T_{\text{sky}}^4 - \epsilon_{\text{sfc}} \sigma T_{\text{sfc}}^4$$

where the shortwave contribution represented by the first two terms (in braces), denoted as  $R_{\text{sun}}$ , accounts for both the direct solar beam and diffuse scattering over the full upper (sky) hemisphere. In both terms  $\mu$  is the solar zenith angle cosine,  $S_o$  is the solar constant,  $S_i$  is an empirical parameter for diffuse scattering, and  $\tau$  is the atmospheric vertical optical depth assumed known either from onsite measurements or from other existing models. Other quantities in eq (9) are respectively the (known) surface emissivity,  $\epsilon_{\text{sfc}}$ , and the sky emissivity,  $\epsilon_{\text{sky}}$ , which is modeled as a function of the ambient air temperature and relative humidity using expressions discussed in appendix A. Note in eq (9) that we explicitly define the upwelling surface radiation,  $R_{\text{sfc}} = -\epsilon_{\text{sfc}}(\sigma T_{\text{sfc}})^4$ , as negative since it is always directed upward and away from the surface. Also we will later have occasion to approximate the “sky” temperature as being equal to the ambient air temperature (i.e.,  $T_{\text{sky}} \sim T_{\text{air}}$ ).

The convective flux,  $H(z,t)$ , also called the sensible heat flux, or “eddy” heat flux, is modeled as a function of both the wind speed,  $w(t)$ , and the air surface temperature gradient using the following semi-empirical relationship:

$$H(0,t) = K(w) \frac{T_{\text{air}}(t) - T_{\text{sfc}}(t)}{\Delta z_{\text{ref}}} \quad (10)$$

where  $T_{\text{air}}(t)$  is the (known) air temperature and  $K(w)$  is the eddy diffusivity which is a function of the measured wind speed,  $w(t)$ , and can be inferred from boundary layer theory or other empirical models (cf. eq (18) and appendix A). Both the wind speed and air temperature are assumed to be measured at the reference height,  $\Delta z_{\text{ref}}$ , which for convenience, we take to be one meter in the calculations to follow. Note from eq (10) that when  $T_{\text{air}}$  is greater than the surface temperature,  $T_{\text{sfc}}$ , that the direction of the flux is positive (downward, toward the surface, heating) and when  $T_{\text{sfc}}$  is greater than  $T_{\text{air}}$ , the direction of the flux is negative (upward, away from the surface, cooling), all consistent with the stated sign convention.

The subsurface, or soil, conductive heat flux density,  $S(z,t)$ , is modeled in a similar way using the following simple but physically reasonable representation:

$$S(0,t) = c_2 \lambda \frac{T_{\max} - T_{\text{sfc}}(t)}{\Delta z_{\text{not}}} \quad (11)$$

where  $\lambda$  is the soil thermal conductivity and  $T_{\max}$  is the "deep soil" maximum temperature, which is assumed a known constant; and  $c_2$  is an adjustable constant determined in a manner described later. Numerical values for  $\lambda$  and other physical parameters as used here are described in appendix A. Note in eq (11) that when  $T_{\text{sfc}}$  is less than  $T_{\max}$ , the direction of the flux is positive (upward, toward the surface, heating); conversely when  $T_{\text{sfc}}$  is greater than  $T_{\max}$ , the direction of the flux is negative (downward, away from the surface, cooling), all again consistent with the stated sign convention.

Substituting the radiative expression into eq (8) and taking care to account also for both the shortwave reflection and longwave absorption at the surface, we have

$$\rho C_s \frac{dT}{dt} = (1 - r_{\text{sfc}}) R_{\text{sun}} + \epsilon_{\text{sfc}} R_{\text{sky}} - \epsilon_{\text{efc}} \sigma T_{\text{sfc}}^4 + H(0,t) + S(0,t) \quad (12)$$

where  $r_{\text{sfc}}$  is the shortwave surface reflectivity and  $\epsilon_{\text{sfc}}$  is the longwave surface emissivity, which in the second term we have assumed to be equal to the surface absorptivity in accordance with the well-known Kirchhoff approximation.

---

### 3. Equilibrium Surface Fluxes

---

There is some controversy regarding fully rigorous time dependent solutions to eq (12) because the details in the infinitesimal region of the interface are not necessarily well understood. However, for the equilibrium case we have  $dT/dt=0$  and eq (12) can be solved in a number of ways to produce what we will call here the equilibrium solution. That is, setting  $dT/dt=0$  in eq (8) we have immediately

$$R_{eq}(t, T_{eq}) + H_{eq}(t, T_{eq}) + S_{eq}(t, T_{eq}) = 0 \quad (13)$$

where we have inserted the subscript "eq" to make clear that the fluxes represent the equilibrium solutions. We now seek to "balance" eq (13) by finding the particular value(s) of the equilibrium temperature,  $T_{eq}(t)$ , that produce a 0 sum. The approach taken by Rachele and Tunick [1] is based on an iterative scheme to find the value of the sensible heat flux density,  $H_{eq}(t)$ , that minimizes the balance in eq (13). We can, in principle, use these results to express the individual equilibrium fluxes directly in terms of the so-determined equilibrium surface temperature:

$$R_{eq}(t, T_{eq}) = (1 - r_{sfc})R_{sun}(t) + \epsilon_{sfc}R_{sky}(t) - \epsilon_{efc}\sigma T_{eq}^4(t) \quad (14)$$

$$S_{eq}(t, T_{eq}) = c_2 \lambda \frac{T_{max} - T_{eq}(t)}{\Delta z_{not}} \quad (15)$$

$$H_{eq}(t, T_{eq}) = K(w) \frac{T_{air} - T_{eq}(t)}{\Delta z_{ref}} \quad (16)$$

where all parameters remain as defined in earlier expressions. Some examples of how the method might work using measured data and the above formulation are shown in figure 3.

The plots in figure 3 are divided into three groups—upper, middle, and lower—and are based on data gathered from a set of special experiments performed at the White Sands Missile Range (WSMR) by Anderson and Chenault [5] during a 3-day period of fair weather conditions in the late fall (Julian days 306, 307, 308). As shown in the upper plots, the measured data included air temperature, wind speed, relative humidity, and in this case, the measured surface temperature obtained from an IR (non-contact) radiometer. As can be inferred from inspection, the weather during the 3 days was reasonably free of any adverse events and showed a general tendency toward increasing surface and air temperatures. The only direct evidence of any cloud

cover is the “glitch” in surface temperature during the middle of the second day which correlates with a similar event in the solar measurement (middle plots). The wind showed a slow decline during the first 24 h and then remained near a steady value (about 2 m/s) for the remainder of the experiment. The relative humidity (shown 1/10 scale in fig. 3) consistently increased steadily during the night to a maximum of around 60 percent and decreased steadily during the day to a minimum of around 20 percent, roughly synchronized 12 h out of phase with the air temperature.

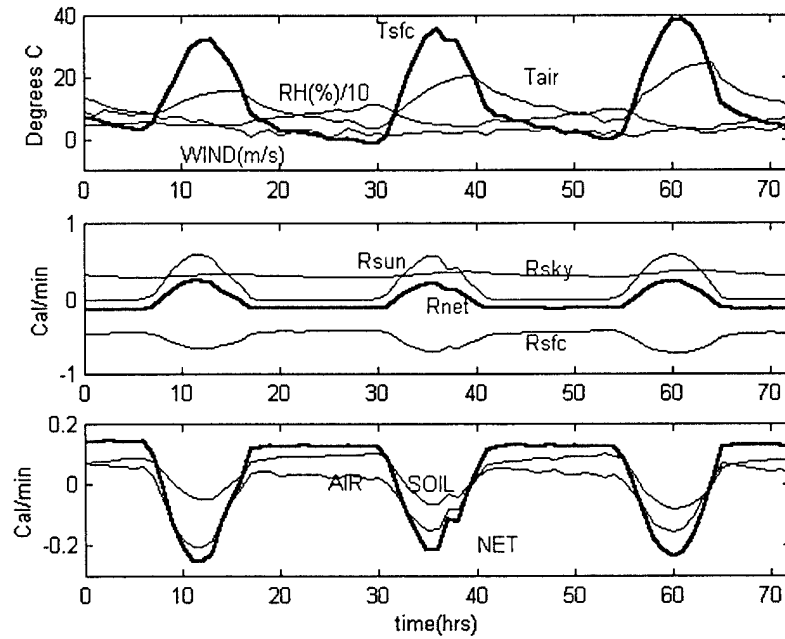


Figure 3. DAY-24 meteorological input and modeled fluxes.

For these experiments the shortwave solar input was measured directly and is shown in the middle plots of figure 3 where the previously mentioned “glitch” (due presumably to a passing cloud during the middle of the second day) is also evident. A comparison of the measured solar data with the model of eq (8) yielded an estimate of  $\tau=0.215$  for the atmospheric optical depth, which is reasonable for the particular site and season. Although it is hard to discern from the plots the trend was toward a steady, but small, increase in solar input with time. Shown also in the middle plots are modeled downwelling and upwelling longwave radiative fluxes from the sky and surface as derived from the above formulation based on the measured air and surface temperatures. Note that the modeled downwelling longwave sky radiation is nearly constant but does show some variation due to



the changing relative humidity. The upwelling (surface) radiation is strongly correlated with the surface temperature and is generally larger than the downwelling (sky) counterpart which is the main mechanism causing the surface to cool at night. The bold trace in the middle set of plots is the net radiative flux as determined from the sum of all three radiative contributions, both shortwave and longwave. It is this net radiative flux that is sometimes referred to as the "forcing" term that drives the temperature changes. This forcing is generally opposed by the reaction fluxes from the air and subsurface (i.e., S and H) which we have shown in the lower set of plots along with the net contributions formed by the sum of the two. We note for this particular case that the soil heat flux was generally larger (in magnitude) than the air heat flux at night but less during the day; however, this aspect of the modeling process is dependent upon the particular parameterization scheme used and is probably the greatest uncertainty in modeling the equilibrium fluxes.

To elaborate on the final point made in the preceding paragraph, it is clear that although we have presumed the surface and subsurface as a simple homogeneous layer, the real world is far more complicated and actually beyond physical description in a rigorous sense. Our solution to dealing with this important practical problem lies in determining the adjustable parameter,  $c_2$ , introduced in eq (11). In our adaptation we use the a-posteriori initial measured air-to-surface temperature difference to adjust the value of  $c_2$  such as to force the equilibrium to zero. That is, from eq (13) and (15) we have

$$c_2 = \frac{R_{eq}(t_o, T_{mea}) + H_{eq}(t_o, T_{mea})}{\frac{\lambda}{\Delta z_{not}} [T_{max} - T_{mea}(t_o)]} \quad (17)$$

where  $T_{mea} [=T_{mea}(t_o)]$ , is the measured initial surface temperature which we assume to be at least approximately equal to the equilibrium temperature. Once  $c_2$  is determined from the initial conditions, the value thus obtained is maintained constant throughout the full 3-day period for which the model was run.

The particular choice made here in forcing the equilibrium balance by adjusting the soil heat flux is not the only option available. In fact the particular value obtained in this manner is strongly dependent upon the values chosen for eddy diffusivity,  $K(w)$ , introduced in eq (10) and which we model as (see also appendix A):

$$K(w) = \frac{1}{c_1} K_o \left( \frac{w(t) + w_o}{w_1} \right)^{1/2} \quad (18)$$

where  $K_o$  ( $=10.50 \text{ w} \cdot \text{m}^{-1} \cdot \text{K}^{-1}$ ) is the zero point eddy diffusivity derived from wind tunnel experiments and  $c_1$  is another semi-empirical constant to account for the effect of the local topography. We assume here that our  $c_1$  parameter can be associated with a surface roughness parameter ( $c_1 \sim \text{Ln}(z_{\text{ruf}}/z_o)$ ), commonly used to account for the effect of local terrain features on the vertical wind profile. In the initial testing of the model, we found a value of  $z_{\text{ruf}} = 20$  (cm) to give the best overall comparisons with the a-posterioria data and this value was used throughout.

One way of actually implementing eq (17) to determine  $c_2$  if the measured initial surface temperature is not known is shown in figure 4.

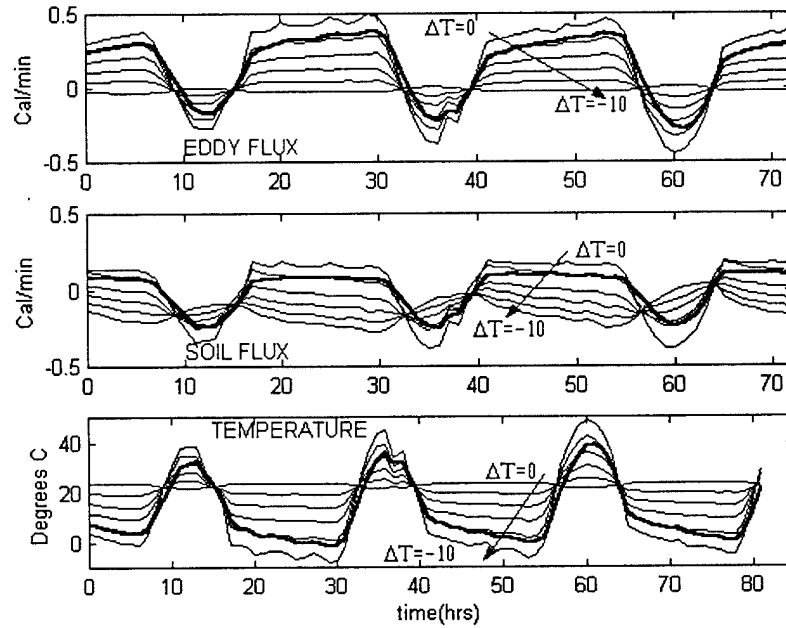


Figure 4. DAY-24 effect of soil thermal properties.

The middle set of plots in figure 4 refer to the soil heat flux,  $S$ , and the upper set refers to the sensible heat flux,  $H$  as determined from eq (15) and (16) assuming the actual (measured) surface temperatures to be nearly equal to the equilibrium temperatures. The various subplots in each case refer to guesses of the initial air-to-surface temperature difference [i.e.,  $\Delta T = T_{\text{air}} - T_{\text{sfc}}$ ] ranging in value from  $-10$  to  $0$  °C in steps of  $2.0$  °C. Since the initialization begins at nighttime, we restrict our guesses to the inversion case. For each guess we calculate a new value of  $c_2$  based on eq (17). The dark solid line refers to the "correct" value based on the measured surface temperature. In this particular example the extreme case for  $\Delta T = -10$  °C for the soil heat flux results in a nearly flat curve near zero and progresses in a more or less monotonic trend upward to the other extreme near the  $0.50$  maximum for  $\Delta T = 0$ . For this particular case an inversion of  $\Delta T = -8$  °C represents the optimum fit which, from eq (17), gives a value of  $1.35$  for  $c_2$  which, in turn, corresponds to an "effective" thermal conductivity of  $0.0041$  cal/mK<sup>-1</sup>. However, this fitting procedure cannot be accomplished blindly because one needs also to look at the effect on the sensible heat flux which in this particular case also yielded a reasonable curve, mainly because of our choice for  $c_1$  in eq (18). The lowermost plots in figure 4 represent the corresponding modeled surface temperatures and are discussed later in section 4.

## 4. Equilibrium Surface Temperature

Although it is simple enough to calculate the surface radiation term directly, it is convenient for computational purposes to "linearize" the energy balance expression by expanding the surface radiation term in a Taylor series and approximating as follows [4];

$$\begin{aligned} R_{sfc} &= \epsilon_{sfc} \sigma T_{sfc}^4 \\ \dots &= \epsilon_{sfc} \sigma [T_o^4 + \frac{\partial T^4}{\partial T} (T - T_o) \dots + \text{higher order terms}] \\ \dots &\approx \epsilon_{sfc} \sigma [T_{max}^4 + 4T_{max}^3 (T_{sfc} - T_{max})] \end{aligned} \quad (19)$$

where, following the usual approach, we have chosen to make the expansion about  $T_{max}$ , the (constant) deep soil temperature. Thus, the "linearized" version of eq (12), utilizing eq (19) for the surface radiation becomes

$$\begin{aligned} \rho C_s \frac{dT}{dt} &= (1 - r_{sfc}) R_{sun} + \epsilon_{sfc} R_{sky} - \epsilon_{efc} \sigma [T_{max}^4 + 4(T_{max}^3 (T - T_{max}))] \\ &+ \frac{K(w)}{\Delta z_{ref}} (T - T_{air}) + c_2 \frac{\lambda}{\Delta z_{not}} (T - T_{max}) \end{aligned} \quad (20)$$

where we have also substituted eq (10) and (11) for the last two terms. The equilibrium solution can be found by setting  $dT/dt=0$  in which case eq (20) can be solved immediately to yield

$$T_{eq}(t) = \frac{(1 - r_{sfc}) R_{sun}(t) + \epsilon_{sfc} R_{sky}(t) + \epsilon_{sfc} \sigma T_{max}^4 + K(w) T_{max} / \Delta z_{max} + T_{air}(t) / \Delta z_{ref}}{4 \epsilon_{sfc} \sigma T_{max}^3 + \frac{K(w)}{\Delta z_{ref}} + c_1 \frac{\lambda_{sub}}{\Delta z_{max}}} \quad (21)$$

where all quantities on the right are known either from onsite measurement or from the various parameterization schemes documented in appendix A. Thus eq (21) yields an immediate determination of the equilibrium surface temperature without the need for extensive reiteration.

As an example, we show the equilibrium solutions in the lowermost set plots in figure 4 (previous section). It is interesting to note in figure 4 that the effect of the soil flux parameter,  $c_2$ , as represented by the inversion values, is to *lower* the nighttime minimum and at the same time to *raise* the daytime maximum which is a consequence of the relationship between the convective and conductive fluxes. In figure 4 we also show (in bold) the remotely measured surface

temperature which seems to match best with an initial inversion of  $-8^{\circ}\text{C}$  which was actually near the observed value of  $-7.9^{\circ}\text{C}$ . Note further that the equilibrium values also seem to accurately model the steady increase in surface temperature as observed over the three day period. The results here are surprising in that results work as well as they do. It is in fact something of a paradox that the time-independent solutions do even a reasonable job in modeling the time dependent scenario. Some insight as to why this is true (or not true) is given in the next section.

## 5. Time Dependence

Although it is tempting to assume the equilibrium temperature to be the same as the actual surface temperature; this is not necessarily true. To find the actual time-dependent temperature we would ordinarily need to start over with the time dependent version of eq (8) and proceed directly with a numerical solution. However, there is more insight to be gained by examining the theoretical relationship between the actual solutions (i.e.,  $dT/dt \neq 0$ ) and the equilibrium solutions (i.e.,  $dT/dt = 0$ ).

We start by first subtracting the equilibrium solutions represented by eq (13), from the time dependent solutions represented by eq (8) to obtain

$$\rho C_s \left. \frac{dT}{dt} \right|_{t=\tau} = \{R(t) - R_{eq}(\tau)\} + \{H(t) - H_{eq}(\tau)\} + \{S(t) - S_{eq}(\tau)\} \quad (22)$$

which is, of course, valid since the equilibrium solution sums to zero.

In eq (22), we have introduced the dummy time parameter,  $\tau$ , to avoid confusion with the independent time variable,  $t$ . In this context we need to think of the equilibrium values at any time,  $\tau$ , as constants based upon the equilibrium fluxes, but not intrinsically dependent on time, per se. Note however that it is understood that the derivative is to be evaluated at  $t=\tau$ . We next perform the term-by-term subtractions using the basic forms for the various fluxes. This operation results in some cancellations of terms and we ultimately arrive at the following final expression:

$$\left. \frac{d\{T(t) - T_{eq}(\tau)\}}{dt} \right|_{t=\tau} = -\frac{1}{\rho C_s} \left\{ 4\sigma T_{max}^3 + \frac{c_2 \lambda}{\Delta z_{max}} + \frac{K(w)}{\Delta z_{ref}} \right\} \{T(t) - T_{eq}(\tau)\} \quad (23)$$

where, for a given wind speed, each of the three terms inside the first set of brackets are constants; thus eq (23) can be integrated immediately to yield

$$\Delta T(t) = (\Delta T)_o \exp - \left\{ \frac{1}{\tau_{sfc}} + \frac{1}{\tau_{sub}} + \frac{1}{\tau_{air}} \right\} t \quad (24)$$

where  $\Delta T_o$  is the difference between the actual time dependent temperature and the equilibrium temperature [i.e.,  $(\Delta T)_o = T(t) - T_{eq}(\tau)$ ]. Thus, eq (24) obviously implies an exponential relaxation process with three distinct time scales defined as follows:

$$\begin{aligned}
\frac{1}{\tau_{\text{sfc}}} &= \frac{4 \sigma T_{\text{max}}^3}{\rho C_s} \\
\frac{1}{\tau_{\text{sub}}} &= \frac{\lambda / \Delta z_{\text{max}}}{\rho C_s} \\
\frac{1}{\tau_{\text{air}}} &= \frac{K(w) / \Delta z_{\text{ref}}}{\rho C_s}
\end{aligned} \tag{25}$$

where the first accounts for radiative processes, the second for conductive processes, and the third for convective processes.

It is interesting to note that our calculations based upon the model and the initial measured data yielded nominal values of around 1.03, 2.10, and 1.51 min for each of the respective processes. The results here indicate that the time-dependent solutions will be different in magnitude from the equilibrium values and there should be some time lag due to the various inertial processes involved and this does seem to be evident upon close examination of the figure 4 data. Although the actual correction of the equilibrium values to account for the time dependence is beyond the scope here, we are pursuing the matter in follow-on work.

---

## 6. Application To IR Scene Generation

---

We next apply the energy balance concept to the problem of IR scene generation. The starting point is some initial thermal array of surface temperatures, or "map," such as that shown in the upper graphic of figure 5, which represents a "thermal" image for the nighttime case near local midnight. The gray scale in this figure is arranged such that the highest temperatures are brighter (i.e., white) and the lower temperatures are darker with a full range of about 10 °C.

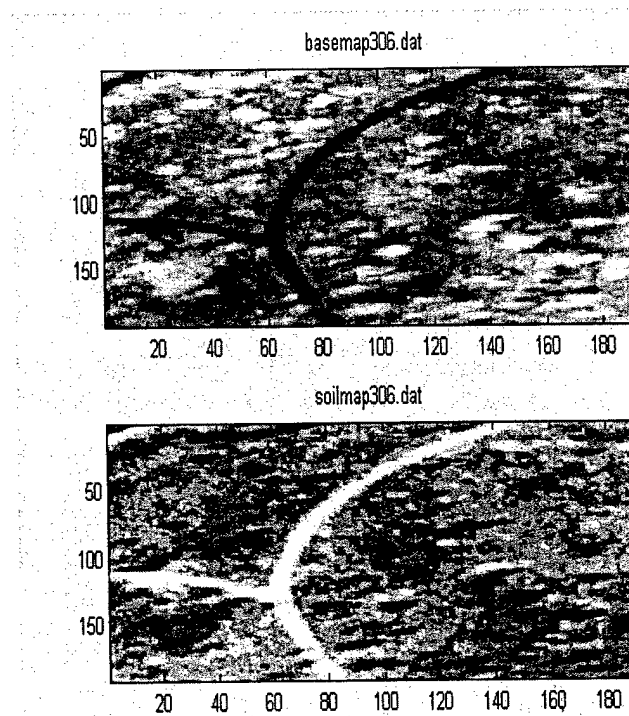


Figure 5. IR scene baseline temperature map (upper) and soil map (lower).

Note in figure 5 the (cooler) dirt road and the relatively hotter vegetation areas that are characteristic of a nighttime scenario. The particular scene in figure 5 is based on a 191 by 191 pixel array corresponding to a spatial resolution of approximately 1 m as viewed from directly above. The data were collected from a real scene which we use here only as an example to demonstrate the method.



The bottom array of figure 5 is a "thermal characterization map" which represents the underlying subsurface thermal properties that were generated using eq (17) and pixel-by-pixel air-to-surface temperature differences estimated from the thermal array. In the bottom array the brighter regions correspond to higher conductivity and the darker regions correspond to lower conductivity. In generating the soil map we have, of course, assumed that the general weather conditions are approximately uniform over the region so that we can use the single "key station" data to model the various fluxes of the energy balance. To complete the example, we also generated estimates of surface reflectivity and emissivity from other imagery of the region. The results for the emissivity and reflectivity characterization are shown in figure. 6.

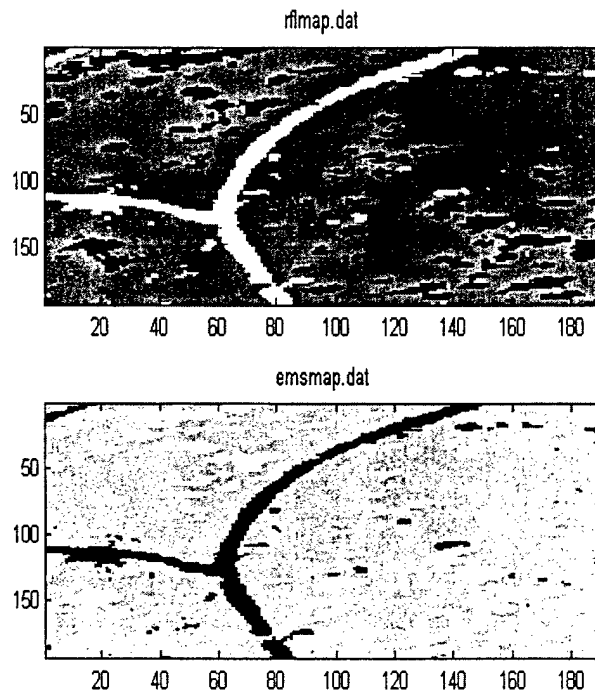


Figure 6. IR scene emissivity map (upper) and reflectivity map (lower).

The characterizations of figure 6 are based, for the most part, on visual band imagery used to discriminate mainly between vegetated and non-vegetated areas and are necessarily crude. In both cases we used three levels to characterize the region corresponding to emissivity values of 0.90 for bare soil, 0.99 for fully vegetated, and 0.95 for mixed and corresponding reflectivity values of 0.20, 0.0, and

0.10, respectively. That is, note in the upper image of Fig. 6 that the (shortwave) reflectivity in the vegetation areas is generally lower than that in bare soil areas as we might expect from the existing database of measurements. Note also from the lower image that the (longwave) emissivity in the vegetation regions is generally higher than that in the bare soil areas, which is also consistent with other studies. The characterization here is necessarily crude and is intended to serve only as an example.

The idea now is to use the onsite point data from the key location as a general indicator of the ambient meteorology, which we then assume to be nearly the same at all nearby pixel locations. The assumption then is that any temperature differences must be due to the underlying surface properties. Results for a full hour-by-hour diurnal cycle are shown in figure. 7.

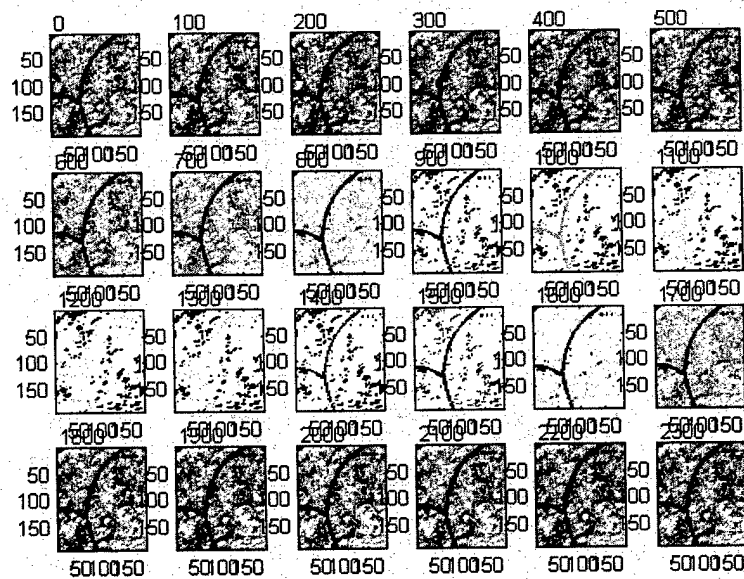


Figure 7. IR scene diurnal cycle.

The arrays in figure 7 begin at nearly midnight and continue through the daytime and evening until midnight the next day, covering roughly the first 24 h of the scenario discussed in connection with figures 3 and 4. As one may expect from examination of the earlier results, the scenes for nighttime, both in the early morning and evening periods, appear to be about the same, indicating slow changes, which is consistent with the meteorological conditions noted earlier. However, the daytime cases are more interesting and, in fact,

show a contrast reversal between the dirt road and background between about 0900 and 1500 hrs including the neutral event at 1000 and 1400 hrs where the contrast reduces to near zero, making the dirt road nearly undetectable. Although there are many quantitative details that need to be worked out, we believe that the results here give a reasonable qualitative picture of reality for a wide variety of applications. Further studies are in progress to compare results with more detailed models.

---

## 7. Summary

---

The surface temperature results for the single site example compare favorably with measurements provided, indicating that we made responsible choices for the various empirical parameters. This statement applies both to the various fluxes which compare favorably with other such studies in the literature and the surface temperature results which agree with data from our own experiments at WSMR. Further development and experimentation is needed to establish the accuracy of our empirical methods for modeling the underlying soil properties under various meteorological conditions. Although appearing realistic, results for the IR scene generation need to be viewed with some caution as we have not yet included atmospheric effects due to turbulence and aerosol-induced obscuration which we plan for the future.

---

## 8. References

---

1. Rachele, H. and A. Tunick, "Energy Balance for Imagery and Electro-magnetic Propagation," *Journal of Applied Meteorology*, 33:8 (1994): pp. 964-976.
2. Sutherland, R.A., "An Objective Nocturnal Temperature Forecasting Model," *Journal of Applied Meteorology*, 19.3 (1980): pp. 247-255.
3. Stull, R.B., *An Introduction to Boundary Layer Meteorology*, Kluwer Academic Publishers: Dordrecht, Netherlands, 1988.
4. Jacobs, P.A., *Thermal Infrared Characterization of Ground Targets and Backgrounds*, published by SPIE-The International Society for Optical Engineering: Bellingham, WA, 1996.
5. Anderson, L. and T. Chenault, "Preliminary Results of DAY-24 Model Validation Experiment," internal briefing: unpublished, 1999.

---

## Appendix A. Parameter Definitions

---

This appendix supplies details of the particular parameterization schemes used to mode the various energy fluxes and physical parameters, including subsurface (soil) thermal properties, eddy convection parameters, solar shortwave radiation, sky and surface longwave emission, and surface moisture evaporation. There is often a mix of units used throughout the literature, and it is worthwhile to keep the following conversions and definitions in mind:

$$1 \text{ Calorie} = 4.19002 \text{ Joules}$$

$$1 \text{ Langley} = 1 \text{ Calorie/minute} = 698.3366 \text{ watt/m}^2$$

$$1 \text{ mb (millibar)} = 10 \text{ mPa (milliPascal)}$$

$$S_0 = \text{Solar constant} = 1.99 \text{ Langley} = 1353 \text{ watt/m}^2$$

$$L_v = \text{latent heat of vaporization} = 2.45 * 10^6 \text{ Joule} \cdot \text{kg}^{-1}$$

$$R_g = \text{universal gas constant} = 287.04 \text{ Joule} \cdot \text{K}^{-1} \cdot \text{kg}^{-1}$$

$$R_v = \text{gas constant for water vapor} = 461.5 \text{ Joule} \cdot \text{K}^{-1} \cdot \text{kg}^{-1}$$

$$\sigma_{sb} = \text{StefanBoltzmanConstant} = 5.67 * 10^{-8} \text{ Watt} \cdot \text{m}^{-2} \cdot \text{K}^{-4}$$

Most of the above definitions are derived from the standard texts, such as those by Stull [3] and Jacobs. [4]

We start with the subsurface parameters which first appear in eq (11) and which we model as a function of soil moisture using the following empirically determined expressions:

*thermal conductivity :*

$$\lambda(\chi) = 0.001 + 0.004 \chi \dots (\text{cal} \cdot \text{cm}^{-1} \cdot \text{sec}^{-1} \cdot \text{K}^{-1})$$

*specific heat :*

$$\rho C(\chi) = 0.27 + 1.0 \chi^{1/2} \dots (\text{cal} \cdot \text{cm}^{-3} \cdot \text{K}^{-1}) \quad (\text{A1})$$

*diffusivity :*

$$\alpha(\chi) = \frac{\lambda(\chi)}{\rho C(\chi)} \dots (\text{sec}^{-1} \cdot \text{cm}^{-2})$$

where  $\chi$  is the fractional soil moisture content and  $\rho$  is the soil bulk density. In practice the actual formulation is overridden by the use of the reference parameter  $\Delta z_{\max}$  and the adjustable parameter  $c_2$  in eq (11); however the expressions do give us some type of check with physical entities. In the Rachele-Tunick [1] model, the soil heat flux is modeled directly as

$$S(t) = (T_{sfc} - T_o) \frac{\lambda}{2\alpha^{1/2}} \sin\left[\frac{\pi}{12}(t(\text{hr}) - t_o)\right] + S_o \quad (\text{A2})$$

where  $T_o$ ,  $t_o$ , and  $S_o$  are empirical parameters derived from the a.posterioria data.

The eddy diffusion coefficient first introduced in eq (10) to determine the sensible heat flux density is modeled as a function of wind speed using the following empirically determined expression:

$$K(w) = \frac{1}{c_1} K_o \left(\frac{w + w_o}{w_1}\right)^{1/2}, K_o = 10.50 \text{ watt} \cdot \text{m}^{-1} \cdot \text{K}^{-1} \cdot \quad (\text{A3})$$

where the parameter  $K_o$  is empirically derived from wind tunnel data,  $w$  (m/s) is the measured wind speed,  $w_o$  (=0.25 m/s) represents the measurement stall speed,  $w_1$  is a wind scaling parameter taken here to be unity, mainly to keep the units consistent, and  $c_1$  is an empirical parameter related to the local terrain roughness as  $c_1 = \ln(z_{ruf}/z_o)$  and for the site here has a numerical value of 2.95 [=Ln 20]. In the Rachele-Tunick version [1], the eddy diffusion coefficient is not used directly but is implicit in their air-to-surface temperature difference formulation expressed as

$$T_{\text{air}} - T_{\text{sfc}} = \frac{T^*}{k} F_\chi(z/L) \quad (\text{A4})$$

where  $k$  is the dimensionless von karman constant,  $T^*$  and  $L$  are scaling parameters, and  $F_\chi(z/L)$  is a scaling function and also a dependent on the local roughness,  $z_{ruf}$ , the form of which is determined from similarity theory.

The sky emissivity, first used in eq (9) is modeled as a function of the ambient pressure, temperature, and humidity as:

*Sky emissivity (dimension less):*

$$\epsilon_{\text{sky}} = \frac{P(\text{hPa})}{101.3} [0.60 + 0.06 \sqrt{e_{\text{vap}}(\text{hPa})}] \quad (\text{A5})$$

where  $P(\text{hPa})$  is the ambient atmospheric pressure and  $e_{\text{vap}}$  is the ambient water vapor pressure:

*Ambient vapor pressure:*

$$\epsilon_{\text{vap}} = \frac{\text{RH}(\%)}{100} (1.831 \cdot 10^{-9}) T_{\text{abs}} \exp(0.06 T_{\text{abs}}) \dots (\text{hPa}) \quad (\text{A6})$$

where  $RH$  (%) is the ambient relative humidity (in percent) and  $T_{abs}$  is the (absolute) ambient air temperature.

In many models the effect of surface water evaporation is parameterized as an equivalent energy flux density, usually designated as  $LE$  and as being proportional to the sensible heat flux. This suggests a new parameterization defining the combined effect of sensible and latent heat,  $H'$  ( $=H+LE$ ), modeled as

$$H'(w, S_{cc}) = \frac{S_{cc} + \gamma}{X_{wet} S_{cc} + \gamma} H(w) \quad (A7)$$

where  $w$  (m/s) is the ambient wind speed and  $H(w)$  is the sensible heat flux density (no evaporation),  $\gamma$  is the psychrometric constant ( $=0.0004 \text{ K}^{-1}$ ), and  $X_{wet}$  is a dimensionless empirical parameter varying from a value of 0.0 for a completely dry surface to a value of about 1.25 for a nearly saturated surface. In eq (A7) the quantity  $S_{cc}$  is the slope of the saturation vapor curve and given by

$$S_{cc} = 0.622 \frac{L_{evap} q_{sat}}{R_{gas} T_{abs}^4} \dots (K^{-1}) \quad (A8)$$

where  $T_{abs}$  is again the (absolute) ambient air temperature,  $R_{gas}$  is the universal gas constant,  $L_{evap}$  is the latent heat of vaporization (see above definitions list), and  $Q_{sat}$  is the saturation specific humidity given by

$$q_{sat} = 0.622 \frac{e_{sat}}{P} \dots (hPa) \quad (A9)$$

where  $e_{sat}$  is given by eq (A6) and  $P$  is again the ambient pressure.

We next turn to the modeling of the shortwave radiation originating from the direct sun rays and and diffuse sky scattering. The solar zenith Cosine,  $\mu$ , is dependent solely upon the sun-earth geometry and is modeled in the usual manner as

*Solar zenith angle [ $\mu = \cos(\theta)$ ]:*

$$\mu = \sin(\theta_{nlat}) \sin(\delta_{sun}) + \cos(\theta_{nlat}) \cos(\delta_{sun}) \cos(\pi \frac{T_{solar} - 12}{12}) \quad (A10)$$

where  $\theta_{nlat}$  is the measured station latitude referenced positive north,  $T_{solar}$  is the local solar time (hours), and  $\delta_{sun}$  is the solar declination angle can be calculated from the Julian Day,  $J_{DAY}$ , as



*Solar declination angle:*

$$\delta_{\text{sun}} = \delta_{\text{max}} \text{Cos}\left[360\left(\frac{J_{\text{DAY}} - 173}{365}\right)\right] \dots \text{degrees south} \quad (\text{A11})$$

where  $\delta_{\text{max}}$  ( $=23.45^\circ$ ) is the yearly minimum which occurs on Julian day 173. The local solar time,  $T_{\text{solar}}$ , is referenced such that the value  $T_{\text{solar}}=12$  (hours) corresponds to the maximum of eq (A10) which defines the station local noon. The relationship between solar time and Universal Coordinated Time (UTC) often used as the standard in modeling is

*Universal Coordinated Time:*

$$T_{\text{solar}} (\text{hours}) = \text{UTC}(\text{hours}) + \frac{\varphi_{\text{lon}} (\text{degrees})}{15} \quad (\text{A12})$$

where  $\varphi_{\text{lon}}$  is the station longitude (0 to  $\pm 180^\circ$ ) measured as positive progressing eastward, and negative progressing westward from the prime meridian at Greenwich, UK. The solar constant,  $S_o$ , is a function of the earth-sun distance which undergoes some variation throughout the year and is modeled as

$$S_o(J_{\text{DAY}}) = \bar{S}_o \left\{ 1 + 0.338 \text{Cos}\left[\frac{2\pi(J_{\text{DAY}} - 3)}{365}\right] \right\} \dots (\text{watt} \cdot \text{m}^{-2}) \quad (\text{A13})$$

where  $S_o$  is the mean solar constant ( $1353 \text{ watt} \cdot \text{m}^{-2}$ ).

---

## Distribution

---

	Copies
OASD C3I RM 3D174 J BUCHHEISTER 6000 DEFENSE PENTAGON WASHINGTON DC 20301-6000	1
OUSD(AT)/S&T AIR WARFARE RM 3E139 R MUTZELBURG 3090 DEFENSE PENTAGON WASHINGTON DC 20301-3090	1
OUSD(AT)/S&T LAND WARFARE RM 3B1060 A VIILU 3090 DEFENSE PENTAGON WASHINGTON DC 20310-3090	1
UNDER SEC OF THE ARMY DUSA OR ROOM 2E660 102 ARMY PENTAGON WASHINGTON DC 20310-0102	1
ACQUSTN LOGISTICS & TCHNLGY SAAL ZP ROOM 2E661 ASST SECY ARMY 103 ARMY PENTAGON WASHINGTON DC 20310-0103	1
ACQUSTN LOGISTICS & TCHNLGY SAAL ZS ROOM 3E448 ASST SECY ARMY 103 ARMY PENTAGON WASHINGTON DC 20310-0103	1
DIRECTOR FORCE DEVELOPMENT DAPR FDZ ROOM 3A522 460 ARMY PENTAGON WASHINGTON DC 20310-0460	1
US ARMY DEV TEST COM CSTE DTC TT T APG MD 21005-5055	1
US ARMY EVALUATION CENTER CSTE AEC SVE R BOWEN 4120 SUSQUEHANNA AVE APG MD 21005-3013	1
US ARMY EVALUATION CENTER CSTE AEC SVE S R POLIMADEI 4120 SUSQUEHANNA AVE APG MD 21005-3013	1

US ARMY EVALUATION CENTER CSTE AEC SVE L R LAUGHMAN 4120 SUSQUEHANNA AVE APG MD 21005-3013	1
US ARMY RESEARCH LAB AMSRL SL DR WADE APG MD 21005-5068	1
US ARMY RESEARCH LAB AMSRL SL J BEILFUSS APG MD 21005-5068	1
US ARMY RESEARCH LAB AMSRL SL B L ROACH APG MD 21005-5068	1
US ARMY RESEARCH LAB AMSRL SL B J FRANZ APG MD 21005-5068	1
US ARMY RESEARCH LAB AMSRL SL BA M RITONDO APG MD 21005-5068	1
US ARMY RESEARCH LAB AMSRL SL BD J MORRISSEY APG MD 21005-5068	1
US ARMY RESEARCH LAB AMSRL SL BE DR TANENBAUM APG MD 21005-5068	1
US ARMY RESEARCH LAB AMSRL SL BG D BELY APG MD 21005-5068	1
US ARMY RESEARCH LAB AMSRL SL BN D FARENWALD APG MD 21005-5068	1
US ARMY RESEARCH LAB AMSRL SL E DR STARKS APG MD 21005-5068	1
US ARMY RESEARCH LAB AMSRL SL EC E PANUSKA APG MD 21005-5068	1

US ARMY RESEARCH LAB AMSRL SL EM DR FEENEY APG MD 21005-5068	1
US ARMY RESEARCH LAB AMSRL SL EI J NOWAK FT MONMOUTH NJ 07703-5601	1
US ARMY TRADOC ANL CTR ATRC W A KEINTZ WSMR NM 88002-5502	1
US ARMY RESEARCH LAB AMSRL SL E C HOPPER WSMR NM 88002-5513	1
US ARMY RESEARCH LAB AMSRL SL EA R ELLIOTT WSMR NM 88002-5513	1
US ARMY RESEARCH LAB R FLORES AMSRL SL EM WSMR NM 88002-5513	1
US ARMY RESEARCH LAB AMSRL SL E MR J PALOMO WSMR NM 88002-5513	1
DEFENSE TECH INFO CENTER DTIC OCA 8725 JOHN J KINGMAN RD STE 0944 FT BELVOIR VA 22060-6218	2
HQDA DAMO FDT 400 ARMY PENTAGON WASHINGTON DC 20310-0460	1
US ARMY MATERIEL CMD AMCRDA TF COMM GENERAL 5001 EISENHOWER AVE ALEXANDRIA VA 22333-0001	1

INST FOR ADVNCD TCHNLGY THE UNIV OF TEXAS AT AUSTIN PO BOX 202797 AUSTIN TX 78720-2797	1
DARPA SPECIAL PROJECTS OFF J CARLINI 3701 N FAIRFAX DR ARLINGTON VA 22203-1714	1
US MILITARY ACADEMY MATH SCI CTR EXC THAYER HALL MAJ HUBER MADN MSCE WEST POINT NY 10996-1786	1
HQDA ODCSPER DAPE MR RM 2C733 300 ARMY PENTAGON WASHINGTON DC 20301-0300	1
US ARMY ARMAMENT RDEC AMSTAARTD M FISETTE B1 PICATINNY ARSENAL NJ 07806-5000	1
US ARMY MISSILE RDEC AMSMI RD DR MCCORKLE REDSTONE ARSENAL AL 35898-5240	1
NATICK SOLDIER CENTER SBCN T P BRANDLER KANSAS STREET NATICK MA 01760-5056	1
US ARMY TANK AUTOMTV RDEC AMSTA TR J CHAPIN WARREN MI 48397-5000	1
US ARMY INFO SYS ENGRG CMD AMSEL IE TD DR F JENIA FT HUACHUCA AZ 85613-5300	1
US ARMY RESEARCH LAB AMSRL D DR SMITH 2800 POWDER MILL RD ADELPHI MD 20783-1197	1
US ARMY RESEARCH LAB AMSRL CI AI R RECORDS MGMT 2800 POWDER MILL RD ADELPHI MD 20783-1145	1

US ARMY RESEARCH LAB AMSRL CI LL 2800 POWDER MILL RD ADELPHI MD 20783-1145	3
US ARMY SIM TRNG INST CMD AMSTI CG DR M MACEDONIA 12350 RESEARCH PKWY ORLANDO FL 32826-3726	1
US ARMY TRADOC BATTLE LAB INTEG TECH & CONCEPTS DIR ATCD B FT MONROE VA 23651-5000	1
US ARMY RESEARCH OFFICE 4300 S MIAMI BLVD RESEARCH TRIANGLE PARK NC 27709	1
SBCCOM RDEC AMSSB RTD J ZARZYCKI 5183 BLACKHAWK RD APG MD 21010-5424	1
US ARMY RESEARCH LAB AMSRL CI LP BLDG 305 APG MD 210055068	2
US ARMY RESEARCH LAB AMSRL SL EM RA SUTHERLAND WSMR NM 88002-5501	5
Record Copy	1
<b>TOTAL</b>	<b>59</b>